

**Constructing the Square-Like Copper Cluster to Boost C-C  
Coupling for CO<sub>2</sub> Electroreduction to Ethylene**

Journal:	<i>Journal of Materials Chemistry A</i>
Manuscript ID	TA-ART-06-2023-003630.R1
Article Type:	Paper
Date Submitted by the Author:	20-Jul-2023
Complete List of Authors:	Zhao, Tiantian; Harbin Normal University, Chemistry Yan, Tingyu; Harbin Normal University Sun, Yuting; Harbin Normal University, Chemistry Wang, Zhongxu; Harbin Normal University, Chemistry Cai, Qinghai; Harbin Normal University, chemistry and chemical engineering Zhao, Jing-Xiang; Harbin Normal University, Chemistry Chen, Zhongfang; University of Puerto Rico, Chemistry

**Constructing the Square-Like Copper Cluster to Boost C-C Coupling for CO<sub>2</sub>  
Electroreduction to Ethylene**

Tiantian Zhao,<sup>1</sup> Tingyu Yan,<sup>1</sup> Yuting Sun,<sup>1</sup> Zhongxu Wang,<sup>1</sup> Qinghai Cai,<sup>1</sup> Jingxiang  
Zhao<sup>1,\*</sup>, Zhongfang Chen<sup>2,\*</sup>

<sup>1</sup> *College of Chemistry and Chemical Engineering, and Key Laboratory of Photonic  
and Electronic Bandgap Materials, Ministry of Education, Harbin Normal University,  
Harbin 150025, China*

<sup>2</sup> *Department of Chemistry, University of Puerto Rico, Rio Piedras Campus, San Juan,  
Puerto Rico 00931, USA*

\* To whom correspondence should be addressed. Email: [zhaojingxiang@hrbnu.edu.cn](mailto:zhaojingxiang@hrbnu.edu.cn)  
(J. Z.); [zhongfang.chen1@upr.edu](mailto:zhongfang.chen1@upr.edu) (Z.C.)

**Abstract:** The CO<sub>2</sub> electroreduction reaction (CO<sub>2</sub>ER) to ethylene (C<sub>2</sub>H<sub>4</sub>) offers the dual promise of lowering CO<sub>2</sub> emission while storing energy from renewable electricity, in which the development of highly efficient electrocatalysts is of great significance. Herein, by means of density functional theory (DFT) computations, we designed an electrocatalyst for CO<sub>2</sub>-to-C<sub>2</sub>H<sub>4</sub> conversion by anchoring the Cu<sub>5</sub> cluster supported on the MoS<sub>2</sub> monolayer with the S monovacancy (Cu<sub>5</sub>@MoS<sub>2</sub>). Our results revealed that one Cu atom of the Cu<sub>5</sub> cluster was embedded into the framework of the defective MoS<sub>2</sub> monolayer, while the other four Cu atoms form a square-like island over the substrate surface. Interestingly, the C–C coupling between two \*CO species can easily occur on the unique square-like active site with a low kinetic barrier of 0.56 eV to form the key \*C<sub>2</sub>O<sub>2</sub> intermediate, which can then be hydrogenated to the C<sub>2</sub>H<sub>4</sub> product with a very low limiting potential (−0.32 eV). Significantly, the alkaline condition (pH = 13) is beneficial to further promote C<sub>2</sub>H<sub>4</sub> synthesis. Our work may offer a new avenue to precisely modulate the structures of the Cu clusters for converting CO<sub>2</sub> into high-value target products.

## 1. Introduction

Electrochemical reduction of carbon dioxide (CO<sub>2</sub>ER) into value-added fuels and chemicals using excess renewable electricity has emerged as a promising strategy to address energy and environmental challenges.<sup>1-3</sup> Various hydrocarbons can be produced through CO<sub>2</sub>ER, including methane (CH<sub>4</sub>), formic acid (HCOOH), ethylene (C<sub>2</sub>H<sub>4</sub>), and ethanol (C<sub>2</sub>H<sub>5</sub>OH).<sup>4</sup> Among these hydrocarbons, C<sub>2</sub>H<sub>4</sub> holds particular significance in industrial applications due to its high value, transportability, and wide range of use in the production of plastics, solvents, and cosmetics.<sup>5-7</sup> However, the CO<sub>2</sub>-to-C<sub>2</sub>H<sub>4</sub> conversion suffers from extremely low selectivity and catalytic activity due to the following substantial challenges:<sup>8-11</sup> 1) the competition with the inevitable hydrogen evolution reaction (HER); 2) the higher thermodynamic potential required for the formation of C<sub>2</sub>H<sub>4</sub> compared to monocarbon (C<sub>1</sub>) compounds, since the C<sub>2</sub>H<sub>4</sub> formation involves a complex 12e<sup>-</sup> pathway ( $2\text{CO}_2 + 12\text{H}^+ + 12\text{e}^- \rightarrow \text{C}_2\text{H}_4 + 4\text{H}_2\text{O}$ ) and a multifaceted reaction network; 3) the difficult C-C coupling reaction between adjacent \*CO(H) adsorbates, characterized by slow kinetics. To overcome these challenges, it is crucial to develop high performance electrocatalysts capable of achieving high selectivity at low potentials for the efficient production of C<sub>2</sub>H<sub>4</sub> through CO<sub>2</sub>ER.

To date, copper (Cu) has been widely recognized as a promising catalyst for the production of multicarbon (C<sub>2+</sub>) compounds, primarily due to its moderate adsorption strength with \*CO intermediate.<sup>12-15</sup> For example, Liu's group reported that Cu-based nanoneedles and grain boundary can promote the C-C coupling and enhance the

catalytic activity of CO<sub>2</sub>ER to C<sub>2</sub> products.<sup>16-19</sup> However, the efficiency and selectivity of Cu-based catalysts for C<sub>2+</sub> products are far from satisfactory due to their high overpotentials, multiple products, inadequate selectivity, and poor stability under reaction conditions.<sup>20-22</sup> Especially, the surface structure of Cu crystals significantly influences C-C coupling reactions.<sup>23-25</sup> For example, Cu(100) has been found to favor C<sub>2</sub>H<sub>4</sub> formation, while CH<sub>4</sub> is preferentially generated from CO<sub>2</sub>ER on Cu(111) surface.<sup>26-29</sup> Consequently, developing novel Cu-based catalysts with high selectivity, activity, stability, and cost-effectiveness for the electrocatalytic conversion of CO<sub>2</sub> to C<sub>2</sub>H<sub>4</sub> remains an appealing yet formidable challenge.

Note that the supported metal clusters (SMCs) have recently emerged as a special type of heterogeneous catalysts, comprising metal clusters stabilized on solid supports to serve as effective catalytic sites.<sup>30, 31</sup> In particular, these SMCs catalysts possess adjacent metal sites, which exhibit an excellent synergistic effect in catalysis, crucial for achieving superior electrocatalytic performance in a multi-step electrochemical process.<sup>32, 33</sup> For example, Wei *et al.*<sup>34</sup> reported that the reconstituted Cu<sub>4</sub> clusters supported on CeO<sub>2</sub> demonstrate good catalytic performance in electrocatalytic urea synthesis, yielding an average urea yield rate of 52.84 mmol h<sup>-1</sup> g<sub>cat.</sub><sup>-1</sup> at -1.6 V *versus* reversible hydrogen electrode (RHE). Liu *et al.*<sup>35</sup> showed that the Cu clusters supported on quasi-amorphous cobalt sulfide can serve as efficient electrocatalysts for water splitting. Additionally, Ling *et al.*<sup>36</sup> constructed a dual Cu-Fe site by anchoring Cu<sub>5</sub> clusters on the surface of FeS<sub>2</sub>, effectively boosting the H<sub>2</sub>O<sub>2</sub> activation. Furthermore, Xu and coworkers<sup>37</sup> discovered that carbon-supported Cu

clusters can electrochemically convert  $\text{CO}_2$  to  $\text{C}_2\text{H}_5\text{OH}$  with a high Faradaic efficiency of 91% at  $-0.7\text{ V}$  and a low onset potential of  $-0.4\text{ V}$ .

Considering the unique structures and great potential of SMCs in electrocatalysis, we are highly intrigued by their applications in synthesizing  $\text{C}_2\text{H}_4$  from  $\text{CO}_2\text{ER}$ . In this regards, Hori *et al.* reported that the formation of  $\text{C}_2\text{H}_4$  product is sensitively dependent on the surface orientation of the Cu electrode: Cu(100) is especially beneficial to  $\text{C}_2\text{H}_4$  generation.<sup>38</sup> Further theoretical studies revealed that the chemisorbed CO dimer ( $^*\text{C}_2\text{O}_2$ ) is the key intermediate for the C–C coupling on Cu(100), which is primarily attributed to its unique square symmetry structure. Specially,  $^*\text{C}_2\text{O}_2$  is a geometry-sensitive adsorbate, and only square-like sites can lead to suitable  $^*\text{C}_2\text{O}_2$  adsorption configuration with low kinetic barrier. Besides, the amount of charge transfer from the Cu(100) surface (square symmetry formed by four atoms) to the adsorbed  $^*\text{C}_2\text{O}_2$  species is larger than that of the hexagonal-symmetry sites formed by three atoms, which also facilitates the C–C coupling at the square-symmetry surface sites with a low kinetic barrier.<sup>39,40</sup>

Inspired by these above innovative studies on the remarkable performance of Cu-based square-like sites for the  $\text{CO}_2$ -to- $\text{C}_2\text{H}_4$  process, an interesting question arises: can a Cu cluster supported by a suitable substrate, possessing a square-like structure akin to the Cu(100) catalyst, be effectively employed for the reduction of  $\text{CO}_2$  into  $\text{C}_2\text{H}_4$ ? To address this issue, herein, we carried out a systematic density functional theory (DFT) study on the design of Cu-based clusters anchored on defective molybdenum disulfide ( $\text{MoS}_2$ ) monolayer with sulfur (S) vacancies as

effective and highly selective catalysts for the reduction of CO<sub>2</sub> to C<sub>2</sub>H<sub>4</sub>. Notably, S vacancies can naturally occur during the preparation of MoS<sub>2</sub> monolayer,<sup>41-43</sup> and have been widely employed as substrates for anchoring various SCMs, such as Cu,<sup>44-47</sup> Ag,<sup>48</sup> and Pt clusters.<sup>49,50</sup> Especially, MoS<sub>2</sub>-based materials have been proposed as efficient catalysts for CO<sub>2</sub> electrochemical reduction, including the anchored SACs and the exposed edges, in which some C<sub>1</sub> products can be obtained, such as CO, CH<sub>4</sub>, and CH<sub>3</sub>OH.<sup>51-56</sup> To the best of our knowledge, however, there are few reports on generating multicarbon products on these MoS<sub>2</sub>-based catalysts.<sup>57,58</sup>

Our computational results demonstrated that the Cu<sub>5</sub> cluster anchored on an S vacancy site (Cu<sub>5</sub>@MoS<sub>2</sub>) features a square-like structure: one Cu atom is embedded within the S vacancy, while the remaining Cu atoms form a square-like Cu-based island. Moreover, Cu<sub>5</sub>@MoS<sub>2</sub> has excellent structural stability and high electrical conductivity. The square-like sites of Cu<sub>5</sub>@MoS<sub>2</sub> facilitate the C–C coupling reaction between two adsorbed \*CO species to form a \*C<sub>2</sub>O<sub>2</sub> intermediate with a low kinetic barrier of 0.56 eV. Importantly, the \*C<sub>2</sub>O<sub>2</sub> intermediate can be easily reduced to C<sub>2</sub>H<sub>4</sub> with high selectivity, while effectively suppressing competing side reactions. The catalytic activity of Cu<sub>5</sub>@MoS<sub>2</sub> is reflected by its rather lower limiting potential of –0.32 V, which is even less negative than the state-of-the-art Cu(100) benchmark (–0.61 V). More importantly, the activity of Cu<sub>5</sub>@MoS<sub>2</sub> towards the CO<sub>2</sub>-to-C<sub>2</sub>H<sub>4</sub> conversion can be further enhanced by the alkaline conditions according to the constant-potential method. Therefore, Cu<sub>5</sub>@MoS<sub>2</sub> demonstrates compelling

electrocatalytic properties, including high activity, high selectivity, and low cost, for the reduction of CO<sub>2</sub> to C<sub>2</sub>H<sub>4</sub>.

## 2. Computational Methods

All spin-polarized DFT computations were performed by using the Vienna Ab Initio Simulation Package (VASP)<sup>59, 60</sup> with the ion-electron interactions represented by the projector augmented wave (PAW) method.<sup>61, 62</sup> The Perdew-Burke-Ernzerhof (PBE) functional<sup>63</sup> within the generalized gradient approximation (GGA) and a cutoff energy of 550 eV for the plane-wave basis set were employed. To ascertain the accuracy of computations of the PBE functional, we repeated related computations for CO<sub>2</sub>ER on Cu<sub>5</sub>@MoS<sub>2</sub> by using the more reliable revised Perdew-Burke-Ernzerhof (rPBE) functional,<sup>64</sup> and the detailed results were shown in Fig. S1. Small differences between the results of PBE and rPBE functionals guarantee the validity of the conclusions in this work. The Grimme's scheme (DFT+D3)<sup>65</sup> was adopted to treat the van der Waals (vdW) interactions between the adopted species and Cu<sub>5</sub>@MoS<sub>2</sub>. The convergence criterion for the geometrical optimization was set to 0.02 eV/Å in residual force and 10<sup>-5</sup> eV in energy, respectively. The partial charge transfer was computed based on the Bader charge analysis.<sup>66</sup>

The Cu<sub>5</sub>@MoS<sub>2</sub> system was constructed by anchoring a Cu<sub>5</sub> cluster on a 4 × 4 × 1 MoS<sub>2</sub> supercell with an S vacancy. The supercell consists of 16 Mo atoms, 31 S atoms, and 5 Cu atoms. To prevent interactions between periodic images, a vacuum space of 20 Å was included in the system. The Brillouin zone in the reciprocal space of Cu<sub>5</sub>@MoS<sub>2</sub> was sampled using a Monkhorst-Pack k-point mesh with a 3 × 3 × 1

$k$ -point grid. The freestanding  $\text{Cu}_5$  cluster was computed in a  $10 \times 10 \times 10 \text{ \AA}^3$  unit cell with  $5 \times 5 \times 5$  Monkhorst–Pack  $k$ -point meshes.

To assess the thermal stability of  $\text{Cu}_5@ \text{MoS}_2$ , ab initio molecular dynamics (AIMD) simulations were performed in the canonical ensemble (NVT) with the Nose-Hoover thermostat<sup>67</sup> at 300K. The simulations were carried out for 20 ps with a time step of 2 fs. The climbing image nudged elastic band (CI-NEB)<sup>68</sup> was employed to determine the minimum energy pathway for the C-C coupling and compute the kinetic barrier.

The binding energy ( $E_b$ ) of the  $\text{Cu}_5$  cluster on the defective  $\text{MoS}_2$  monolayer was computed by:  $E_b = E(\text{Cu}_5@ \text{MoS}_2) - E(\text{Cu}_5) - E(\text{MoS}_2)$ , where  $E(\text{Cu}_5@ \text{MoS}_2)$ ,  $E(\text{Cu}_5)$ ,  $E(\text{MoS}_2)$  represent the total energies of the  $\text{Cu}_5$  cluster supported on the  $\text{MoS}_2$  monolayer, the isolated  $\text{Cu}_5$  cluster, and the bare  $\text{MoS}_2$  monolayer with an S vacancy, respectively. According to this definition, a more negative  $E_b$  value suggests a stronger interaction.

To explore the catalytic activity of  $\text{Cu}_5@ \text{MoS}_2$  toward  $\text{CO}_2\text{ER}$ , the computational electrode model (CHE) method<sup>69, 70</sup> was employed to compute the free energy diagrams and the limiting potentials of the  $\text{CO}_2$ -to- $\text{C}_2\text{H}_4$  process. The free energy change ( $\Delta G$ ) of each elementary step in  $\text{CO}_2\text{ER}$  can be obtained by the formula:  $\Delta G = \Delta E + \Delta ZPE - T\Delta S + eU$ , where  $\Delta E$  is the reaction energy of reactant and product species adsorbed on the catalyst directly obtained from DFT computations;  $\Delta ZPE$  and  $\Delta S$  represent the differences in zero-point energy and entropy, respectively, between the adsorbed species and the gas phase molecules at

298.15 K, which can be calculated from the vibrational frequencies.  $U$  was the applied potential. According to the obtained free energy change of each elementary step, the limiting potential ( $U_L$ ) was further computed as follows:  $U_L = -\max(\Delta G_1, \Delta G_2, \Delta G_3, \Delta G_4, \dots, \Delta G_i)/e$ .

To elucidate the reaction mechanism under different electrode potentials, we carried out computations using the constant-potential method, in which the excess charge per unit cell ( $\Delta n$ ) ranging from  $-2.0 e^-$  to  $+2.0 e^-$  with a step size of  $0.5 e^-$  was incrementally introduced. A reference value of 4.6 eV was adopted for the standard hydrogen electrode (SHE). The potential-dependent energy can be calculated by:  $E = E_{DFT} - \Delta n(V_{sol} + \varphi_q)/e$ , where  $E_{DFT}$  is the DFT-calculated energy,  $V_{sol}$  is the electrostatic potential of the bulk electrolyte, and  $-\varphi_q$  is the work function of the charged system. The relation between  $\varphi_q$  and the corresponding electrode potential referenced to the standard hydrogen electrode (SHE) scale is  $U_q(U/SHE) = -4.6V - \varphi_q/e$ . The  $E-U_q$  quadratic form can be written as:  $E(U_q) = -\frac{1}{2}C(U_q - U_0)^2 + E_0$ , where  $U_0$ ,  $C$ , and  $E_0$  are the fitted values of the potential of zero charge (PZC), the capacitance of the corresponding system, and the energy of the system at the PZC, respectively. The fixed potential, referenced to the standard hydrogen electrode (SHE) scale, varies with the pH value. The relationship between the SHE potential ( $U_{SHE}$ ) and the reversible hydrogen electrode (RHE) potential ( $U_{RHE}$ ) is given by  $U_{RHE} = U_{SHE} + 0.0592 \times \text{pH}$ . This equation enables the determination of the RHE potential based on the pH value.

### 3. Results and Discussion

### 3.1. Geometric Structure, Stability, and Electronic Property.

First, we examined the structure and stability of the adsorbed Cu<sub>5</sub> cluster on the S vacancy of the MoS<sub>2</sub> substrate. For the freestanding Cu<sub>5</sub> cluster, both planar and three-dimensional (3D) structures were considered (Fig. S2a), as they are the two lowest energy isomers of the Cu<sub>5</sub> cluster.<sup>71</sup> Then, the two Cu<sub>5</sub> clusters were positioned on various sites of the defective MoS<sub>2</sub> monolayer, including the S vacancy site, the Mo site's top, and the hollow site within the Mo<sub>3</sub>S<sub>3</sub> ring.

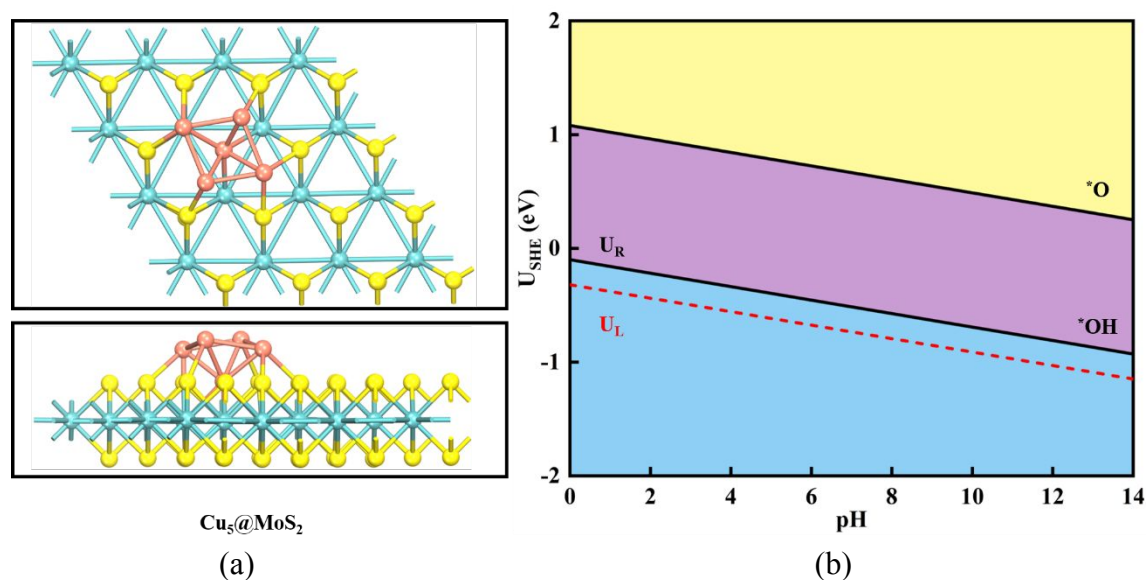
As expected, both of the two Cu<sub>5</sub> clusters exhibit a preference for binding to the S vacancy after full atomic relaxation (Fig. S2b). Interestingly, the binding of the 3D Cu<sub>5</sub> cluster to the defective MoS<sub>2</sub> monolayer is much stronger than that of the planar Cu<sub>5</sub> cluster, as evidenced by their respective  $E_b$  values of  $-5.07$  eV vs  $-4.23$  eV. These values are more negative than the cohesive energy of the bulk Cu materials ( $-3.86$  eV), highlighting the exceptional capability of the S vacancy site within the defective MoS<sub>2</sub> substrate to firmly immobilize Cu<sub>5</sub> clusters. Consequently, the subsequent discussion will primarily focus on the stability and properties of the 3D Cu<sub>5</sub> cluster supported on the defective MoS<sub>2</sub> substrate.

Noteworthy, this configuration allows for the formation of a reverse pentahedral Cu<sub>5</sub> cluster (Fig. 1a). In this arrangement, one Cu atom is fully embedded into the framework of MoS<sub>2</sub> monolayer, occupying the position previously occupied by the removed S atom, and forming three Cu-Mo bonds with lengths of  $2.50$  Å. Meanwhile, the remaining four Cu atoms are positioned outward from the MoS<sub>2</sub> surface, forming a square-like Cu island with Cu-Cu lengths of about  $2.49$  Å,

with the bottom Cu atom binding to the island with a length of 2.32 Å. The square-symmetry surface sites of the Cu<sub>5</sub> cluster result in the particular “double-bridge state” within an identical coordination environment. This configuration is advantageous for the parallel attack and simultaneous activation of two CO<sub>2</sub> molecules. In addition, the appropriate distance of 2.49 Å between adjacent Cu-Cu bridge sites may promote the C-C coupling of carbon-containing intermediates. Obviously, the structural feature of the anchored Cu<sub>5</sub> cluster bear a striking resemblance to that of the Cu(100) slab<sup>72-74</sup> and meet the intrinsic requirements for the electroreduction of CO<sub>2</sub> to C<sub>2</sub>H<sub>4</sub>.

Furthermore, the stability of Cu<sub>5</sub>@MoS<sub>2</sub> was evaluated through AIMD simulations at 300 K for 20 *ps* (Fig. S3), from which we found that the structure of this catalyst can be well maintained, suggesting that the 3D Cu<sub>5</sub> cluster can be firmly anchored to the S-vacancy of the MoS<sub>2</sub> substrate to ensure its high stability. In addition, we examined the electrochemical stability of Cu<sub>5</sub>@MoS<sub>2</sub> by exploring whether its bare surfaces would be covered by \*O/\*OH species in an aqueous solution under operation. To address this, a surface Pourbaix diagram was constructed, which represents the most stable surface structures under realistic conditions.<sup>75, 76</sup> The results revealed that at an electrode potential of 0 V, the Cu<sub>5</sub>@MoS<sub>2</sub> surface is predominantly covered by \*OH species across all pH values. However, upon the application of electrode potential, the \*OH species will be hydrogenated to H<sub>2</sub>O. Importantly, at pH=0, the minimum potential required to remove the surface \*OH species (U<sub>R</sub>) is –0.10 V (Fig. 1b), which is less negative than the limiting potential of CO<sub>2</sub>ER (–0.32 V

as discussed later). Besides, we also computed the dissolution potential ( $U_{\text{diss}}$ , more details are given in Supporting Information) of the Cu active site in  $\text{Cu}_5/\text{MoS}_2$  catalyst at the operating potential of the cathode (*i.e.*, negative overpotential,  $-\eta$ ). Remarkably, the  $U_{\text{diss}}$  of the Cu active site within the anchored  $\text{Cu}_5$  cluster ( $-0.04$  V) is significantly less negative than the ( $-\eta$ ) value of  $\text{CO}_2$ -to- $\text{C}_2\text{H}_4$  on this catalyst ( $\eta = 0.38$  V, see Supporting Information).<sup>77</sup> Consequently, the  $\text{Cu}_5@\text{MoS}_2$  system exhibits excellent electrochemical stability against surface oxidation and can withstand the practical reaction environments of  $\text{CO}_2\text{ER}$  under working conditions. Note that the successful synthesis of Cu clusters on  $\text{MoS}_2$ -based substrates with point defects has been experimentally demonstrated.<sup>44-47</sup> These experimental findings greatly inspired us further to explore the catalytic performance of such systems in  $\text{CO}_2\text{ER}$ .



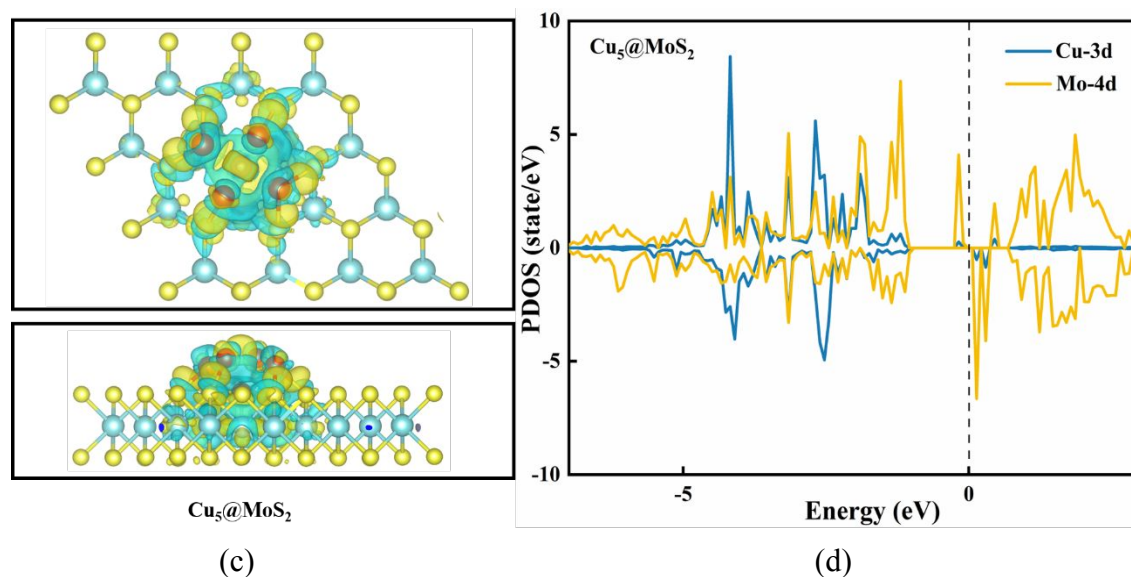


**Fig. 1.** a) Optimized structure of Cu<sub>5</sub>@MoS<sub>2</sub> from both the top and side views. b) Surface Pourbaix diagram of Cu<sub>5</sub>@MoS<sub>2</sub>. The thermodynamically stable states of the surface under SHE and pH values are highlighted by yellow regions for \*O and pink regions for \*OH. The red dashed line represents the limiting potential of CO<sub>2</sub>ER. c) Differential charge density plot of Cu<sub>5</sub>@MoS, with yellow representing electron accumulation and cyan denoting electron depletion. The isosurface value is set to be 0.005 e Å<sup>-3</sup>. d) Spin-polarized partial density of states (PDOS) of the 3d-orbitals of the bottom Cu atom and the 4d-orbitals of the adjacent Mo atoms in the Cu<sub>5</sub>@MoS<sub>2</sub> system.

To gain deep insights into the strong interaction of the Cu<sub>5</sub> cluster on the S-vacancy site of the MoS<sub>2</sub> monolayer, we examined the charge transfer and the orbital hybridization between them. As shown in Fig. 1c, we observed partial oxidation of the Cu atom that is captured by the S vacancy site, leading to the formation of three strong-polarized Cu-Mo bonds through the hybridization of Cu-3d and Mo-4d orbitals (Fig. 1d). Moreover, the top four Cu atoms in the adsorbed Cu<sub>5</sub>

cluster carry a nearly identical positive charge of 0.22  $|e|$ , indicating their uniform coordination environments and confirming the square-symmetry feature. This square-symmetry is known to facilitate the transfer of more electrons to the CO<sub>2</sub>ER intermediates. In addition, according to the computed band structure, this pristine MoS<sub>2</sub> substrate exhibits a semiconducting characteristic with a band gap of 1.12 eV (Fig. S4a). Upon the adsorption of the Cu<sub>5</sub> cluster adsorption, however, some impurity states are introduced into the band structure (Fig. S4b), greatly reducing the band gap to 0.11 eV and thus resulting in an enhanced electrical conductivity, which is beneficial for the process of CO<sub>2</sub>ER.

### 3.2. CO<sub>2</sub>ER Performance on Cu<sub>5</sub>/MoS<sub>2</sub>.

Efficient CO<sub>2</sub> electroreduction (CO<sub>2</sub>ER) relies on successfully activating CO<sub>2</sub> on the catalyst surface. After fully structural relaxation, we found that the C atom of CO<sub>2</sub> is preferable to be adsorbed on the Cu-Cu bridge site with the lengths of 2.06 Å, while its two O atoms bind with the Cu top site with the lengths of 2.11 Å. Compared with the linear structure of the free CO<sub>2</sub> molecule, the adsorbed \*CO<sub>2</sub> experiences a C-O bond length elongation of 0.06, and a bending of the O-C-O angle is by 40° (Fig. S5a). These structural changes indicate the sufficient activation of \*CO<sub>2</sub> on the Cu<sub>5</sub>/MoS<sub>2</sub> system. Notably, the explicit solvent can further increase the \*CO<sub>2</sub> adsorption strength by about 0.45 eV (Fig. S5b), while a small change ( $\leq 0.05$  V) can be observed for the computed limiting potential by different solvent effects (Table S1), which has been widely regarded as a criterion to estimate the catalytic activity of CO<sub>2</sub>ER on a given catalyst. It is easily understood that the CO<sub>2</sub> activation originates from substantial

charge transfer from the Cu-3d orbitals into the  $\text{CO}_2-2\pi^*$  orbitals (0.54 |e|) and strong hybridizations between the Cu-3d orbitals and the C/O-2p orbitals (Fig. S5c). This substantial charge transfer and orbital hybridization contribute to the effective capture and activation of  $\text{CO}_2$  on  $\text{Cu}_5@\text{MoS}_2$ , which will likely facilitate its subsequent reduction.

Having established the sufficient activation of the  $\text{CO}_2$  molecule, we evaluated the catalytic activity and the product distribution of  $\text{CO}_2\text{ER}$  on the  $\text{Cu}_5@\text{MoS}_2$  catalyst. In order to reveal the reaction mechanisms, we employed the CHE method to identify the reaction pathway with the lowest positive free energy change between any two elementary steps, which corresponds to the most favorable reaction pathway. Then, the applied voltage required for the entire reaction to become exergonic, known as the limiting potential ( $U_L$ ), was determined.

### 3.2.1. $\text{CO}_2\text{ER}$ leading to $\text{C}_1$ products.

By considering various possible reaction pathways (Fig. 2a), we thoroughly examined the feasibility of  $\text{CO}_2$  electroreduction to  $\text{C}_1$  products on the  $\text{Cu}_5@\text{MoS}_2$  catalyst and identified the most favorable reaction pathway (Fig. 2b).



Based on the computed free energy changes of all elementary steps along the lowest-energy pathway, we revealed the following sequence of reactions. Firstly, one O atom of CO<sub>2</sub> is hydrogenated to generate \*COOH species with an uphill free energy of 0.22 eV. Note that this energy barrier is lower than that observed on the Cu(211) surface (0.41 eV)<sup>78</sup> and the Cu (100) surface (0.52 eV)<sup>24</sup>. Subsequently, the \*COOH intermediate reacts with a second (H<sup>+</sup> + e<sup>-</sup>) pair, resulting in the formation of (\*CO + H<sub>2</sub>O). Remarkably, the \*CO formation is slightly endothermic by 0.18 eV, which is significantly lower than that of the competitive \*HCOOH formation ( $\Delta G = 0.54$  eV). Moreover, due to the strong adsorption strength (-0.96 eV), the formed \*CO undergoes further hydrogenation to generate the \*CHO species, and this step only requires a small energy input of 0.32 eV, which is lower by 0.56 eV than that of the competing \*COH formation. In the following step, the (H<sup>+</sup> + e<sup>-</sup>) pair continually attacks the C site of \*CHO, leading to the formation of \*CH<sub>2</sub>O and \*CH<sub>3</sub>O after two consecutive hydrogenation steps. Importantly, these reactions occur downhill in the free energy profile by 0.54 and 0.26 eV, respectively. Next, the hydrogenation of \*CH<sub>3</sub>O intermediate induces the C–O bond breaking, resulting in the release of the CH<sub>4</sub> product. This step is exothermic by 0.88 eV in the free energy diagram. Meanwhile, the remaining O atom on the Cu-Cu bridge with a length of 1.78 Å undergoes further hydrogenation to form \*OH with the  $\Delta G$  of -1.21 eV, followed by its subsequent hydrogenation to generate the second H<sub>2</sub>O. However, this step of \*OH → \*H<sub>2</sub>O is endothermic by 0.91 eV due to the strong \*OH adsorption on Cu<sub>5</sub>@MoS<sub>2</sub> (-4.76 eV).

Overall, in the CO<sub>2</sub>-to-CH<sub>4</sub> process, the \*OH hydrogenation is identified as the potential-determining step (PDS) due to its maximum  $\Delta G$  value of 0.91 V (Fig. 2), corresponding to the U<sub>L</sub> of -0.91 V, which is even more negative than that observed on the Cu(211) slab (-0.74 V)<sup>70</sup> and the competitive HER process (-0.86 V). Therefore, the formation of CH<sub>4</sub> as a product is unlikely to be achieved on the Cu<sub>5</sub>@MoS<sub>2</sub> surface. Instead, we expect \*CO species to be the main product at low potential due to its remarkable binding strength with this catalyst (-0.96 eV).

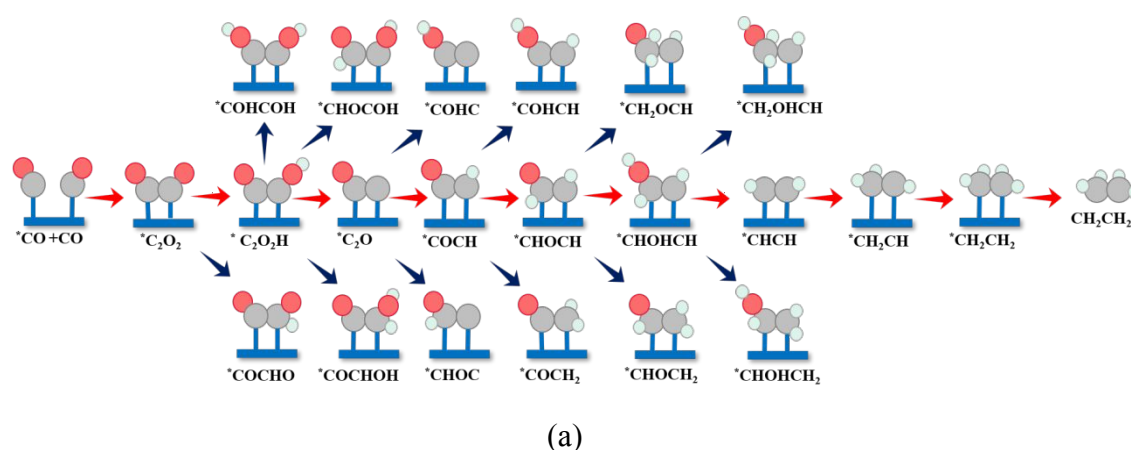
### 3.2.2. CO<sub>2</sub>ER leading to C<sub>2</sub> products.

Due to the unique “double-bridged” active sites in the Cu<sub>5</sub>@MoS<sub>2</sub> system, after \*CO is adsorbed on a Cu-Cu bridge site, the other Cu-Cu bridge site can continue to activate and convert the CO<sub>2</sub> molecule. Interestingly, the hydrogenation free energies of CO<sub>2</sub> and \*COOH are greatly reduced with the increase of CO<sub>2</sub>, calculated to be 0.02 and -0.48 eV, respectively (Fig. S6a). As a result, two separate chemisorbed \*CO species on the two opposing bridge sites of Cu<sub>5</sub>@MoS<sub>2</sub> are formed. Previous studies<sup>24, 65</sup> have indicated that the C-C coupling step *via* \*CO dimerization to \*C<sub>2</sub>O<sub>2</sub> intermediate is crucial for C<sub>2</sub>H<sub>4</sub> generation on Cu(100) surface during CO<sub>2</sub>ER. Therefore, we explored the potential for coupling the two \*CO species on Cu<sub>5</sub>@MoS<sub>2</sub>. Excitingly, the kinetic barrier for this coupling reaction is only 0.56 eV (Fig. S6b), even lower than that of on Cu(100) surface (0.82 eV),<sup>29</sup> highlighting the unique advantage of Cu-based square-like sites in promoting C-C coupling.

In addition to \*CO dimerization, we also considered two other common C-C coupling steps, namely, (\*CHO + \*CO) and (\*CHO + \*CHO) couplings, for

comparison. However, as shown in Fig. S7, the computed kinetic barriers for these two coupling reactions, 1.72 and 0.99 eV, respectively, are significantly higher than that of the CO dimerization (0.56 eV). Thus, the C–C coupling between  $^*\text{CO}$  species is kinetically favorable and feasible on  $\text{Cu}_5@\text{MoS}_2$ . A similar phenomenon was also observed on  $\text{Cu}(100)$  slab.<sup>29</sup>

We proceeded to investigate the thermodynamics of the subsequent hydrogenation steps of the  $^*\text{C}_2\text{O}_2$  intermediate to form  $\text{C}_2$  products, following the successful C–C coupling through  $^*\text{CO}$  dimerization. In this process, various reaction pathways were considered, including O–H bond formation, C–H bond formation, and C–OH bond breaking processes (Fig. 3a). By determining the most stable structure for each intermediate, we obtained the free energy diagram along the most energetically favorable pathway for  $\text{CO}_2\text{ER}$  to  $\text{C}_2$  products, as depicted in Fig. 3b. For comparison, we summarized the free energy changes along other less favorable pathways in Table S2.



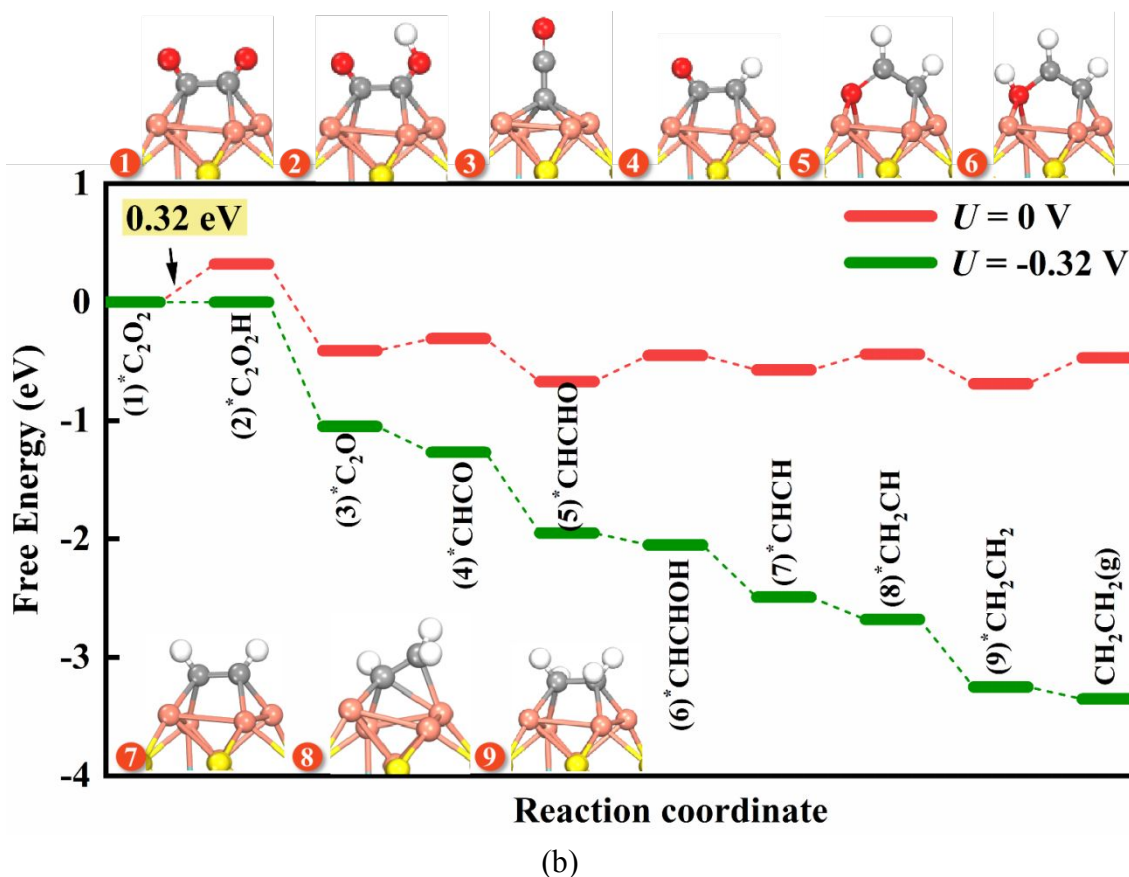


**Fig. 3.** (a) Possible reaction pathways considered for CO<sub>2</sub>ER to C<sub>2</sub> products. (b) Free energy diagram for C<sub>2</sub>H<sub>4</sub> generation along the most favorable pathway, along with the corresponding configurations of the reaction intermediates.

Our results showed that the (H<sup>+</sup> + e<sup>-</sup>) pairs preferentially attack one of the oxygen atom of \*C<sub>2</sub>O<sub>2</sub>, leading to the formation of \*C<sub>2</sub>O<sub>2</sub>H, and then continuously approaches this oxygen atom, resulting in the generation of \*C<sub>2</sub>O and the release of a H<sub>2</sub>O molecule. Remarkably, the formation of \*C<sub>2</sub>O<sub>2</sub>H is slightly uphill by 0.32 eV, whereas \*C<sub>2</sub>O formation is downhill by 0.73 eV in the free energy profile. Note that the \*C<sub>2</sub>O species is vertically adsorbed on the fourfold hollow site of the Cu<sub>5</sub>@MoS<sub>2</sub> system *via* the C-end pattern with a length of about 2.00 Å.

In the following steps, the hydrogenation of  $^*C_2O$  preferentially proceeds along the  $^*C_2O \rightarrow ^*CHCO \rightarrow ^*CHCHO \rightarrow ^*CHCHOH$  pathways, with  $\Delta G$  values of 0.10,  $-0.36$ , and  $0.22$  eV, respectively. Once  $^*CHCHOH$  is formed, the subsequent pathway bifurcates into two routes:  $C_2H_4$ -formation and  $C_2H_5OH$ -formation. Interestingly, we found that the formation of  $^*CHCH$  intermediate, which can be regarded as the precursor of  $C_2H_4$  product, is more favorable than  $^*CH_2CHOH$  and  $^*CHCH_2OH$ , with the  $\Delta G$  value lower by  $0.25$  and  $0.49$  eV, respectively. This  $\Delta G$  difference suggests that  $C_2H_4$  is likely the main product of  $CO_2ER$  on the  $Cu_5@MoS_2$  system. After the formation of  $^*CHCH$  species, the production of  $C_2H_4$  proceeds smoothly through two successive hydrogenation steps, with corresponding free energy changes of  $0.13$  and  $-0.25$  eV, respectively. Finally, the formed  $C_2H_4$  molecule is released from the  $Cu_5@MoS_2$  surface with a low energy input of  $0.22$  eV, allowing the regeneration of the catalyst for subsequent catalytic cycles.

Now, a comprehensive reaction pathway for  $CO_2ER$  to  $C_2H_4$  on the  $Cu_5@MoS_2$  catalyst surface can be summarized as follows:  $CO_2 + ^* \rightarrow ^*COOH \rightarrow ^*CO \rightarrow ^*C_2O_2 \rightarrow ^*C_2O_2H \rightarrow ^*C_2O \rightarrow ^*CHCO \rightarrow ^*CHCHO \rightarrow ^*CHCHOH \rightarrow ^*CHCH \rightarrow ^*CH_2CH \rightarrow ^*CH_2CH_2 \rightarrow CH_2CH_2 + ^*$ . In this pathway, the hydrogenation of  $^*C_2O_2$  is the PDS with a free energy change of  $0.32$  eV. According to the CHE model, the smallest applied potential of  $-0.32$  V required to make all elementary reactions exergonic, that is, the limiting potential is  $-0.32$  V (Fig. 3), which is less negative than the  $Cu(100)$  benchmark ( $-0.61$  V),<sup>24</sup> suggesting the higher catalytic activity of our designed  $Cu_5@MoS_2$  catalyst in promoting the  $CO_2ER$  process and facilitating  $C_2H_4$  generation.

Furthermore, we computed the activation barriers to simulate the mechanism of  $C_2H_4$  formation from a kinetic perspective by using one water assisted hydrogen shuttling model, which has been extensively adopted to compute the barriers of electrochemical  $CO_2$  reduction<sup>79-81</sup> We found that the largest activation barrier of 0.73 eV locates at the protonation of  $*C_2O_2$  (Fig. S8), which is higher than that of  $*CO$  dimerization (0.56 eV), but is lower than 0.75 eV that corresponds to a fast electrochemical process.<sup>82</sup> Thus,  $Cu_5@MoS_2$  is facile for the electrochemical reduction of  $CO_2$  to  $C_2H_4$  product kinetically.

In addition, considering that the  $CO_2ER$  takes place in aqueous solutions, we also evaluated the solvent effect on the catalytic activity using the implicit solvation model implemented in VASPsol.<sup>83</sup> It can be clearly seen from Fig. S9 that the PDS with solvent effect still locates at the  $*C_2O_2$  hydrogenation with the limiting potential of  $-0.30$  V, which is comparable to that of without solvent effect of  $-0.32$  V, indicating that the solvent environment is not an obstacle to impair the excellent catalytic activity of  $Cu_5@MoS_2$  towards  $C_2H_4$  synthesis from the  $CO_2ER$ .

The selectivity of this catalyst toward  $C_2H_4$  production is also noteworthy. For this regard, we examined two major competing reactions, namely the hydrogen evolution reaction (HER) and the formation of  $C_2H_5OH$  on the  $Cu_5@MoS_2$  surface. For HER, the energy input required for  $H_2$  release is significantly higher (0.86 eV) compared with that for  $C_2H_4$  synthesis (0.32 eV). Moreover, the binding strength of the key  $*COOH$  intermediate on the  $Cu_5@MoS_2$  catalyst is much stronger ( $-2.79$  eV) than that of  $*H$  species ( $-1.09$  eV), suggesting a preference for the adsorption of

\*COOH species on the active site. These findings indicate the excellent suppression effect of the Cu active sites within the anchored Cu<sub>5</sub> cluster on the competitive HER.

The C<sub>2</sub>H<sub>4</sub> *versus* C<sub>2</sub>H<sub>5</sub>OH selectivity highly depends on the adsorption strength of \*OH on the catalyst surface. The square-like sites of the anchored Cu<sub>5</sub> cluster exhibit a relatively strong \*OH binding, making it more difficult for Cu–O bond breaking compared to O–C bond breaking. As a result, the C<sub>2</sub>H<sub>4</sub> production is thermodynamically more favorable than the C<sub>2</sub>H<sub>5</sub>OH production by at least 0.25 eV (Table S2). The distribution of the two products can be further evaluated by the thermodynamic formula  $\exp[-(\Delta G)/(RT)]$ . In this equation,  $\Delta G$  is the free energy difference for the formation of (\*CHCH + H<sub>2</sub>O) and (\*CH<sub>2</sub>CHOH); here  $\Delta G = 0.25$  eV at T = 298 K. Thus, the C<sub>2</sub>H<sub>4</sub>:C<sub>2</sub>H<sub>5</sub>OH molar ratio is computed to be about  $1.68 \times 10^4:1$  at ambient temperature, suggesting a rather high C<sub>2</sub>H<sub>4</sub> selectivity, thanks to its unique square-like active sites.

### 3.3. pH-dependent CO<sub>2</sub>ER activity.

Although the CHE model has predicted the superior catalytic performance of Cu<sub>5</sub>@MoS<sub>2</sub> for CO<sub>2</sub>ER to C<sub>2</sub>H<sub>4</sub> and also provided insights into the reaction mechanism, it fails to capture the pH-dependent activity due to the cancellation of pH and electrode potential corrections.<sup>84-88</sup> Actually, many experimental studies demonstrated that CO<sub>2</sub>ER activity for C<sub>2</sub>H<sub>4</sub> production on Cu-based catalysts is generally higher under alkaline conditions compared to acidic conditions.<sup>5</sup> Therefore, understanding the pH-dependent activity is crucial in CO<sub>2</sub> electroreduction. Recently, Duan *et al.* successfully addressed this issue by utilizing their constant-potential

method (CPM), which accounts for solvent and constant-potential effects in electrocatalysis to simulate a more realistic environment.<sup>89-93</sup>

To examine the pH impact on the CO<sub>2</sub>ER activity of Cu<sub>5</sub>@MoS<sub>2</sub>, we employed the CPM combined with the implicit solvent model. By analyzing the energetics of CO<sub>2</sub>ER, we obtained the computed total energies of bare Cu<sub>5</sub>@MoS<sub>2</sub> surface and the adsorbed reaction intermediates along the most favorable pathway of the CO<sub>2</sub>-to-C<sub>2</sub>H<sub>4</sub> process as a function of the applied electrode potential (Fig. 4a). Encouragingly, all energy-potential points align well with a quadratic relationship, and the specific fitted data are listed in Table S3. Furthermore, we compiled the computed  $E_{\text{ads}}$  values of these C-based reaction intermediates with respect to the applied potential (in Fig. 4b).

Additionally, we plotted the pH-dependent and potential-dependent contour illustrating the adsorption energies of \*C<sub>2</sub>O<sub>2</sub> on Cu<sub>5</sub>@MoS<sub>2</sub> (Fig. 4c), as this intermediate is closely related to the PDS. Our simulations showed that the adsorption strength of \*C<sub>2</sub>O<sub>2</sub> on the Cu<sub>5</sub>@MoS<sub>2</sub> catalyst increases as the pH increases or the applied potential decreases. For example, at pH = 1, the  $E_{\text{ads}}$  of \*C<sub>2</sub>O<sub>2</sub> is -1.78 eV, while at pH = 13, it rises to -2.59 eV, suggesting that the alkaline conditions enhance the activation of \*C<sub>2</sub>O<sub>2</sub>. Therefore, the CO<sub>2</sub>ER activity of Cu<sub>5</sub>@MoS<sub>2</sub> is indeed pH-dependent. Especially, we found that this catalyst exhibits the highest catalytic activity at pH = 13 (Fig. S10), corresponding to an exceptionally low limiting potential of -0.25 V vs reverse hydrogen electrode (RHE) (Fig. 4d). Notably, due to the strong \*C<sub>2</sub>O<sub>2</sub> adsorption at pH = 13, the PDS turns into the hydrogenation of \*CHCHO to \*CHCHOH.

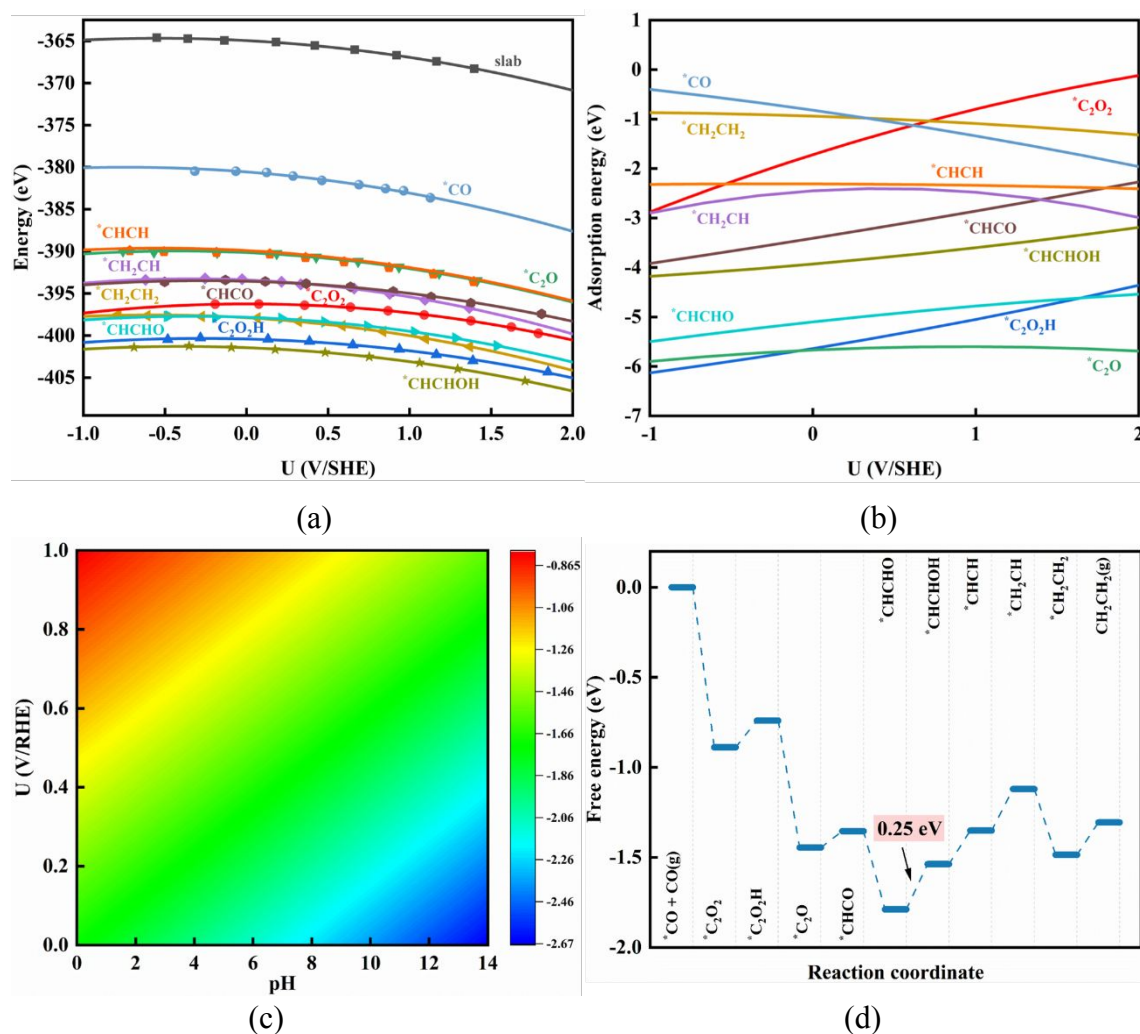


**Fig. 4.** The computed total energies of the  $\text{Cu}_5@\text{MoS}_2$  catalyst and the corresponding reaction intermediates as a function of the applied electrode potential. (b) Adsorption energies of various C-based reaction intermediates as a function of the applied electrode potential. (c) pH-dependent and potential-dependent contour plot of adsorption energies of  $^*\text{C}_2\text{O}_2$  on  $\text{Cu}_5@\text{MoS}_2$  surface. (d) The free energy profile for  $\text{CO}_2$ -to- $\text{C}_2\text{H}_4$  conversion on  $\text{Cu}_5@\text{MoS}_2$  at pH = 13.

### 3.4. Square-Like Active Sites of $\text{Cu}_5@\text{MoS}_2$ vs. Anchored $\text{Cu}_n$ Clusters in $\text{CO}_2$ Electroreduction

To highlight the significance of the square-like active sites of  $\text{Cu}_5@ \text{MoS}_2$  in facilitating  $\text{C}_2\text{H}_4$  production, we also examined the catalytic performance of other anchored  $\text{Cu}_n$  clusters ( $n = 1, 2, 3, 4,$  and  $6$ ) for C–C coupling in  $\text{CO}_2\text{ER}$ . As expected, for a single Cu atom, the C–C coupling is not feasible due to the absence of sufficient active sites. For other Cu clusters, we found that the coupling between two adsorbed CO species is unstable, resulting in their spontaneous optimization into two isolated CO species after full structural relaxation (Fig. S11a).

Furthermore, we computed the kinetic barriers ( $E_{\text{barrier}}$ ) for the C-C coupling *via* the “carbene” mechanism, focusing on the coupling between  $\text{CO}^*$  and  $\text{CHO}^*$  as a representative case. We found the coupling of  $\text{CO}^*$  with  $\text{CHO}^*$  on these Cu clusters is not facile, because their  $E_{\text{barrier}}$  values are larger than 0.75 eV (1.00 to 1.53 eV, Fig. S11b). These results further underscore the distinct advantages of the square-like active sites in  $\text{Cu}_5@ \text{MoS}_2$  for boosting the C-C coupling.

#### 4. Conclusions

In summary, by means of comprehensive DFT computations, we designed a promising  $\text{CO}_2\text{ER}$  catalyst for  $\text{C}_2\text{H}_4$  synthesis by anchoring a 3D  $\text{Cu}_5$  cluster on a defective  $\text{MoS}_2$  monolayer. The S monovacancy enables the formation of a unique square-like active site, which can effectively promote the C-C coupling between two  $^*\text{CO}$  species with a low kinetic barrier of 0.56 eV. Moreover, the resulting  $^*\text{C}_2\text{O}_2$  intermediate can be easily hydrogenated to  $\text{C}_2\text{H}_4$  product with a lower limiting potential ( $-0.32$  V) than the  $\text{Cu}(100)$  benchmark. Importantly, the  $\text{Cu}_5@ \text{MoS}_2$  surface

effectively suppresses side reactions such as HER and the  $\text{CH}_4/\text{C}_2\text{H}_5\text{OH}$  formation, ensuring high selectivity toward  $\text{C}_2\text{H}_4$  production. Notably, the conversion of  $\text{CO}_2$  to  $\text{C}_2\text{H}_4$  is pH-dependent, with the highest catalytic activity observed at pH 13, accompanied by a remarkably low limiting potential of  $-0.25$  V. Our findings not only propose a promising catalyst for  $\text{C}_2\text{H}_4$  synthesis via  $\text{CO}_2\text{ER}$ , but also offer a feasible strategy to design highly-efficient catalysts using anchored sub-nano clusters. This work is expected to inspire more experimental and theoretical studies to explore the potential applications of such catalysts in various other electrochemical reactions.

## NOTES

The authors declare no competing financial interest.

## ACKNOWLEDGEMENT

This work was financially supported in China by the Natural Science Foundation of Heilongjiang Province of China (TD2020B001) and the Natural Science Funds for Distinguished Young Scholar of Heilongjiang Province (No. JC2018004), and in the USA by the Department of Energy, Office of Basic Energy Sciences under Award Number DE-SC0023418.

## References

1. J. Qiao, Y. Liu, F. Hong and J. Zhang, *Chem. Soc. Rev.*, 2014, **43**, 631-675.
2. Y. Y. Birdja, E. Pérez-Gallent, M. C. Figueiredo, A. J. Göttele, F. Calle-Vallejo

- and M. T. M. Koper, *Nat. Energy*, 2019, **4**, 732-745.
3. J.-J. Wang, X.-P. Li, B.-F. Cui, Z. Zhang, X.-F. Hu, J. Ding, Y.-D. Deng, X.-P. Han and W.-B. Hu, *Rare Metals*, 2021, **40**, 3019-3037.
  4. A. N. El Aisnada, M. Miyauchi, M. Liu and A. Yamaguchi, *Mater. Reports: Energy*, 2023, 100190.
  5. X. Chen, Y. Zhao, J. Han and Y. Bu, *ChemPlusChem*, 2023, **88**, e202200370.
  6. H. S. Jeon, S. Kunze, F. Scholten and B. Roldan Cuenya, *ACS Catal.*, 2018, **8**, 531-535.
  7. J.-J. Li and Z.-C. Zhang, *Rare Metals*, 2022, **41**, 723-725.
  8. H. Jung, S. Y. Lee, C. W. Lee, M. K. Cho, D. H. Won, C. Kim, H.-S. Oh, B. K. Min and Y. J. Hwang, *J. Am. Chem. Soc.*, 2019, **141**, 4624-4633.
  9. D. Gao, R. M. Arán-Ais, H. S. Jeon and B. Roldan Cuenya, *Nat. Catal.*, 2019, **2**, 198-210.
  10. K. Jiang, R. B. Sandberg, A. J. Akey, X. Liu, D. C. Bell, J. K. Nørskov, K. Chan and H. Wang, *Nat. Catal.*, 2018, **1**, 111-119.
  11. Z.-Z. Wu, X.-L. Zhang, Z.-Z. Niu, F.-Y. Gao, P.-P. Yang, L.-P. Chi, L. Shi, W.-S. Wei, R. Liu, Z. Chen, S. Hu, X. Zheng and M.-R. Gao, *J. Am. Chem. Soc.*, 2022, **144**, 259-269.
  12. S. Nitopi, E. Bertheussen, S. B. Scott, X. Liu, A. K. Engstfeld, S. Horch, B. Seger, I. E. L. Stephens, K. Chan, C. Hahn, J. K. Nørskov, T. F. Jaramillo and I. Chorkendorff, *Chem. Rev.*, 2019, **119**, 7610-7672.
  13. Z. Ni, H. Liang, Z. Yi, R. Guo, C. Liu, Y. Liu, H. Sun and X. Liu, *Coord. Chem.*

*Rev.*, 2021, **441**, 213983.

14. Y. Zheng, A. Vasileff, X. Zhou, Y. Jiao, M. Jaroniec and S.-Z. Qiao, *J. Am. Chem. Soc.*, 2019, **141**, 7646-7659.

15. J. Yu, J. Wang, Y. Ma, J. Zhou, Y. Wang, P. Lu, J. Yin, R. Ye, Z. Zhu and Z. Fan, *Adv. Funct. Mater.*, 2021, **31**, 2102151.

16. T. Luo, K. Liu, J. Fu, S. Chen, H. Li, J. Hu and M. Liu, *J. Energy. Chem.*, 2022, **70**, 219-223.

17. Y. Zhou, Y. Liang, J. Fu, K. Liu, Q. Chen, X. Wang, H. Li, L. Zhu, J. Hu and H. Pan, *Nano Lett.*, 2022, **22**, 1963-1970.

18. B. Yang, K. Liu, H. Li, C. Liu, J. Fu, H. Li, J. E. Huang, P. Ou, T. Alkayyali and C. Cai, *J. Am. Chem. Soc.*, 2022, **144**, 3039-3049.

19. H. Li, H. Zhou, Y. Zhou, J. Hu, M. Miyauchi, J. Fu and M. Liu, *Chin. J. Catal.*, 2022, **43**, 519-525.

20. A. R. Woldu, Z. Huang, P. Zhao, L. Hu and D. Astruc, *Coord. Chem. Rev.*, 2022, **454**, 214340.

21. B. Sun, M. Dai, S. Cai, H. Cheng, K. Song, Y. Yu and H. Hu, *Fuel*, 2023, **332**, 126114.

22. W. Ma, X. He, W. Wang, S. Xie, Q. Zhang and Y. Wang, *Chem. Soc. Rev.*, 2021, **50**, 12897-12914.

23. F. Hu, L. Yang, Y. Jiang, C. Duan, X. Wang, L. Zeng, X. Lv, D. Duan, Q. Liu, T. Kong, J. Jiang, R. Long and Y. Xiong, *Angew. Chem. Int. Ed.*, 2021, **60**, 26122-26127.

24. Y.-B. Chang, C. Zhang, X.-L. Lu, W. Zhang and T.-B. Lu, *Nano Res.*, 2022, **15**, 195-201.
25. R. B. Sandberg, J. H. Montoya, K. Chan and J. K. Nørskov, *Surf. Sci.*, 2016, **654**, 56-62.
26. Y. Huang, C. W. Ong and B. S. Yeo, *ChemSusChem*, 2018, **11**, 3299-3306.
27. Z. Zhang, L. Bian, H. Tian, Y. Liu, Y. Bando, Y. Yamauchi and Z.-L. Wang, *Small*, 2022, **18**, 2107450.
28. O. Piqué, Q. H. Low, A. D. Handoko, B. S. Yeo and F. Calle-Vallejo, *Angew. Chem. Int. Ed.*, 2021, **60**, 10784-10790.
29. O. Piqué, F. Viñes, F. Illas and F. Calle-Vallejo, *ACS Catal.*, 2020, **10**, 10488-10494.
30. C. Dong, Y. Li, D. Cheng, M. Zhang, J. Liu, Y.-G. Wang, D. Xiao and D. Ma, *ACS Catal.*, 2020, **10**, 11011-11045.
31. M. Peng, C. Dong, R. Gao, D. Xiao, H. Liu and D. Ma, *ACS Central Sci.*, 2021, **7**, 262-273.
32. B. Zhang, Y. Chen, J. Wang, H. Pan and W. Sun, *Adv. Funct. Mater.*, 2022, **32**, 2202227.
33. T. Lu and H. Wang, *Nano Res.*, 2022, **15**, 9764-9778.
34. X. Wei, Y. Liu, X. Zhu, S. Bo, L. Xiao, C. Chen, T. T. T. Nga, Y. He, M. Qiu, C. Xie, D. Wang, Q. Liu, F. Dong, C.-L. Dong, X.-Z. Fu and S. Wang, *Adv. Mater.*, 2023, **35**, 2300020.
35. Y. Liu, Q. Li, R. Si, G.-D. Li, W. Li, D.-P. Liu, D. Wang, L. Sun, Y. Zhang and

- X. Zou, *Adv. Mater.*, 2017, **29**, 1606200.
36. C. Ling, X. Liu, H. Li, X. Wang, H. Gu, K. Wei, M. Li, Y. Shi, H. Ben, G. Zhan, C. Liang, W. Shen, Y. Li, J. Zhao and L. Zhang, *Angew. Chem. Int. Ed.*, 2022, **61**, e202200670.
37. H. Xu, D. Rebolgar, H. He, L. Chong, Y. Liu, C. Liu, C.-J. Sun, T. Li, J. V. Muntean, R. E. Winans, D.-J. Liu and T. Xu, *Nat. Energy*, 2020, **5**, 623-632.
38. Y. Hori, I. Takahashi, O. Koga and N. Hoshi, *J. Mol. Catal. A: Chem.*, 2003, **199**, 39-47.
39. H. Li, Y. Li, M. T. M. Koper and F. Calle-Vallejo, *J. Am. Chem. Soc.*, 2014, **136**, 15694-15701.
40. I. Ledezma-Yanez, E. P. Gallent, M. T. M. Koper and F. Calle-Vallejo, *Catal. Today*, 2016, **262**, 90-94.
41. W. Zhou, X. Zou, S. Najmaei, Z. Liu, Y. Shi, J. Kong, J. Lou, P. M. Ajayan, B. I. Yakobson and J.-C. Idrobo, *Nano Lett.*, 2013, **13**, 2615-2622.
42. F. Bertoldo, R. R. Unocic, Y.-C. Lin, X. Sang, A. A. Puzos, Y. Yu, D. Miakota, C. M. Rouleau, J. Schou, K. S. Thygesen, D. B. Geohegan and S. Canulescu, *ACS Nano*, 2021, **15**, 2858-2868.
43. S. Najmaei, J. Yuan, J. Zhang, P. Ajayan and J. Lou, *Acc. Chem. Res.*, 2015, **48**, 31-40.
44. Y. Han, D. Jing, Y. Luan, C.-J. Wang, M. Kolmer, Z. Fei, M. C. Tringides and J. W. Evans, *J. Phys. Chem. Lett.*, 2022, **13**, 6651-6656.
45. D. Jing, A. Lii-Rosales, K. C. Lai, Q. Li, J. Kim, M. C. Tringides, J. W. Evans

- and P. A. Thiel, *New J. Phys.*, 2020, **22**, 053033.
46. D. Jing, Y. Han, J. W. Evans, M. Kolmer, Z. Fei and M. C. Tringides, *Phys. Rev. Mater.*, 2022, **6**, 094008.
47. G. Shi, L. Yu, X. Ba, X. Zhang, J. Zhou and Y. Yu, *Dalton trans.*, 2017, **46**, 10569-10577.
48. M. Ghosal Chowdhury, L. Sahoo, S. Maity, D. Bain, U. K. Gautam and A. Patra, *ACS Appl. Nano Mater.*, 2022, **5**, 7132-7141.
49. G. Boschetto, S. Carapezzi and A. Todri-Sanial, *ACS App. Electronic Mater.*, 2023, DOI: 10.1021/acsaelm.2c01722.
50. F. Shi, W. Wu, J. Chen and Q. Xu, *Chem. Commun.*, 2021, **57**, 7011-7014.
51. Y. Xie, X. Li, Y. Wang, B. Li, L. Yang, N. Zhao, M. Liu, X. Wang, Y. Yu and J.-M. Liu, *Appl. Surf. Sci.*, 2020, **499**, 143964.
52. Y. Linghu, T. Tong, C. Li and C. Wu, *Appl. Surf. Sci. Appl.*, 2022, **590**, 153001.
53. A. Datar, M. Bar-Sadan and A. Ramasubramaniam, *J. Phys. Chem. C*, 2020, **124**, 20116-20124.
54. K. Kumar, S. Jamnuch, L. Majidi, S. Misal, A. Ahmadiparidari, M. A. Dato, G. E. Sterbinsky, T. Wu, A. Salehi-Khojin and T. A. Pascal, *J. Phys. Chem. Lett.* 2023, **14**, 3222-3229.
55. M. Asadi, B. Kumar, A. Behranginia, B. A. Rosen, A. Baskin, N. Repnin, D. Pisasale, P. Phillips, W. Zhu and R. Haasch, *Nat. commun.*, 2014, **5**, 4470.
56. J. Zhao, D. Liu, F. Wei, W. F. Ip, H. Pan and S. Lin, *Nano Research*, 2023, 1-8. DOI: 10.1007/s12274-023-5718-7.

57. S. A. Francis, J. M. Velazquez, I. M. Ferrer, D. A. Torelli, D. Guevarra, M. T. McDowell, K. Sun, X. Zhou, F. H. Saadi and J. John, *Chem. Mater.*, 2018, **30**, 4902-4908.
58. S. Kang, S. Han and Y. Kang, *ChemSusChem*, 2019, **12**, 2671-2678.
59. G. Kresse and J. Hafner, *Phys. Rev. B*, 1993, **47**, 558-561.
60. G. Kresse and J. Furthmüller, *Phys. Rev. B*, 1996, **54**, 11169-11186.
61. P. E. Blochl, *Phys. Rev. B*, 1994, **50**, 17953-17979.
62. G. Kresse and D. Joubert, *Phys. Rev. B*, 1999, **59**, 1758-1775.
63. J. P. Perdew, K. Burke and M. Ernzerhof, *Phys. Rev. Lett.*, 1996, **77**, 3865-3868.
64. B. Hammer, L. B. Hansen and J. K. Nørskov, *Phys. Rev. B*, 1999, **59**, 7413.
65. S. Grimme, *J. Comput. Chem.*, 2006, **27**, 1787-1799.
66. M. Yu and D. R. Trinkle, *J. Chem. Phys.*, 2011, **134**, 064111.
67. G. J. Martyna, M. L. Klein and M. Tuckerman, *J. Chem. Phys.*, 1992, **97**, 2635-2643.
68. G. Henkelman, B. P. Uberuaga and H. Jónsson, *J. Chem. Phys.*, 2000, **113**, 9901-9904.
69. J. K. Nørskov, J. Rossmeisl, A. Logadottir, L. Lindqvist, J. R. Kitchin, T. Bligaard and H. Jónsson, *J. Phys. Chem. B*, 2004, **108**, 17886-17892.
70. A. A. Peterson, F. Abild-Pedersen, F. Studt, J. Rossmeisl and J. K. Nørskov, *Energy & Environ. Sci.*, 2010, **3**, 1311-1315.
71. P. Calaminici, A. M. Köster, N. Russo and D. R. Salahub, *J. Chem. Phys.*, 1996, **105**, 9546-9556.

72. H. Yang, Y. Wu, Q. Lin, L. Fan, X. Chai, Q. Zhang, J. Liu, C. He and Z. Lin, *Angew. Chem. Int. Ed.*, 2018, **57**, 15476-15480.
73. S. Hanselman, M. T. M. Koper and F. Calle-Vallejo, *ACS Energy Lett.*, 2018, **3**, 1062-1067.
74. K. J. P. Schouten, E. Pérez Gallent and M. T. M. Koper, *ACS Catal.*, 2013, **3**, 1292-1295.
75. V. Sumaria, D. Krishnamurthy and V. Viswanathan, *ACS Catal.*, 2018, **8**, 9034-9042.
76. M. Bajdich, M. García-Mota, A. Vojvodic, J. K. Nørskov and A. T. Bell, *J. Am. Chem. Soc.*, 2013, **135**, 13521-13530.
77. X. Cui, W. An, X. Liu, H. Wang, Y. Men and J. Wang, *Nanoscale*, 2018, **10**, 15262-15272.
78. C. Shi, K. Chan, J. S. Yoo and J. K. Nørskov, *Org. Process. Res. Dev.*, 2016, **20**, 1424-1430.
79. W. Luo, X. Nie, M. J. Janik and A. Asthagiri, *ACS Catal.*, 2016, **6**, 219-229.
80. X. Nie, M. R. Esopi, M. J. Janik and A. Asthagiri, *Angew. Chem.*, 2013, **125**, 2519-2522.
81. X. Nie, W. Luo, M. J. Janik and A. Asthagiri, *J. Catal.*, 2014, **312**, 108-122.
82. C. Shi, K. Chan, J. S. Yoo and J. K. Nørskov, *Org. Process. Res. Dev.*, 2016, **20**, 1424-1430.
83. K. Mathew, R. Sundararaman, K. Letchworth-Weaver, T. Arias and R. G. Hennig, *J. Chem. Phys.*, 2014, **140**.

84. X. Hu, S. Chen, L. Chen, Y. Tian, S. Yao, Z. Lu, X. Zhang and Z. Zhou, *J. Am. Chem. Soc.*, 2022, **144**, 18144-18152.
85. X. Zhang and Z. Zhou, *J. Phys. Chem. C*, 2022, **126**, 3820-3829.
86. T. Liu, Y. Wang and Y. Li, *Adv. Funct. Mater.*, 2022, **32**, 2207110.
87. T. Liu, Y. Jing and Y. Li, *J. Phys. Chem. Lett.*, 2021, **12**, 12230-12234.
88. Y. Sun, Z. Wang, Y. Liu, Q. Cai and J. Zhao, *Inorg. Chem. Front*, 2023, **10**, 2677-2688.
89. Z. Duan and G. Henkelman, *ACS Catal.*, 2019, **9**, 5567-5573.
90. Z. Duan and G. Henkelman, *J. Phys. Chem. C*, 2020, **124**, 12016-12023.
91. Z. Duan and G. Henkelman, *ACS Catal.*, 2020, **10**, 12148-12155.
92. Z. Duan and P. Xiao, *J. Phys. Chem. C*, 2021, **125**, 15243-15250.
93. Z. Duan and G. Henkelman, *ACS Catal.*, 2021, **11**, 14439-14447.